Supporting Information

Mechanical design of the highly porous cuttlebone: a bioceramic hard buoyancy tank for cuttlefish

Ting Yang^, Zian Jia^, Hongshun Chen, Zhifei Deng, Wenkun Liu, Liuni Chen and Ling Li*

Affiliations:
Department of Mechanical Engineering, Virginia Tech, Blacksburg, VA 24060, USA.

^ Equal contributions
* Correspondence to: lingl@vt.edu

www.pnas.org/cgi/doi/10.1073/pnas.2009531117

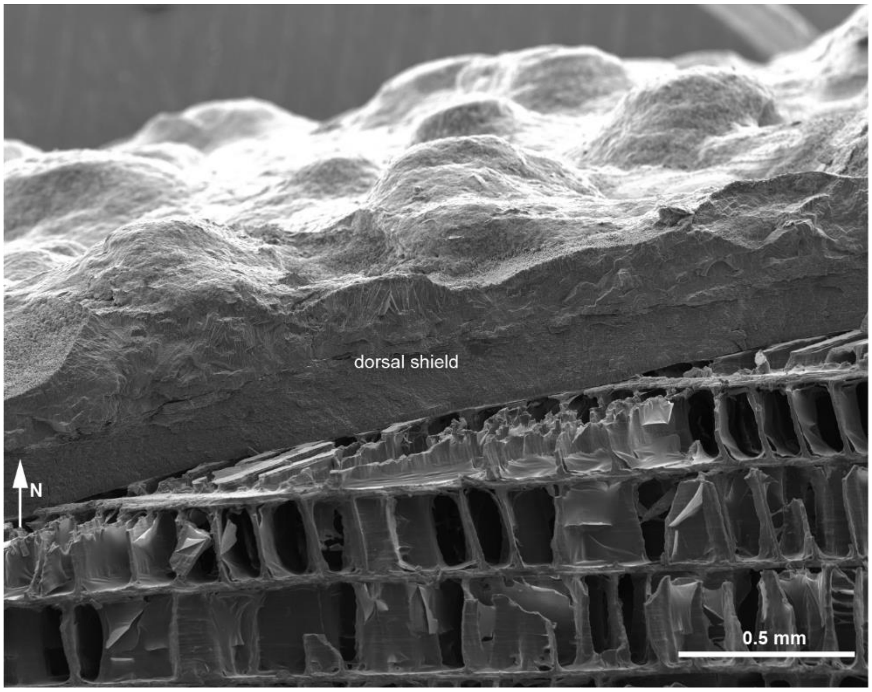

Fig. S1. A cross-sectional SEM image of the dorsal shield in cuttlebone.

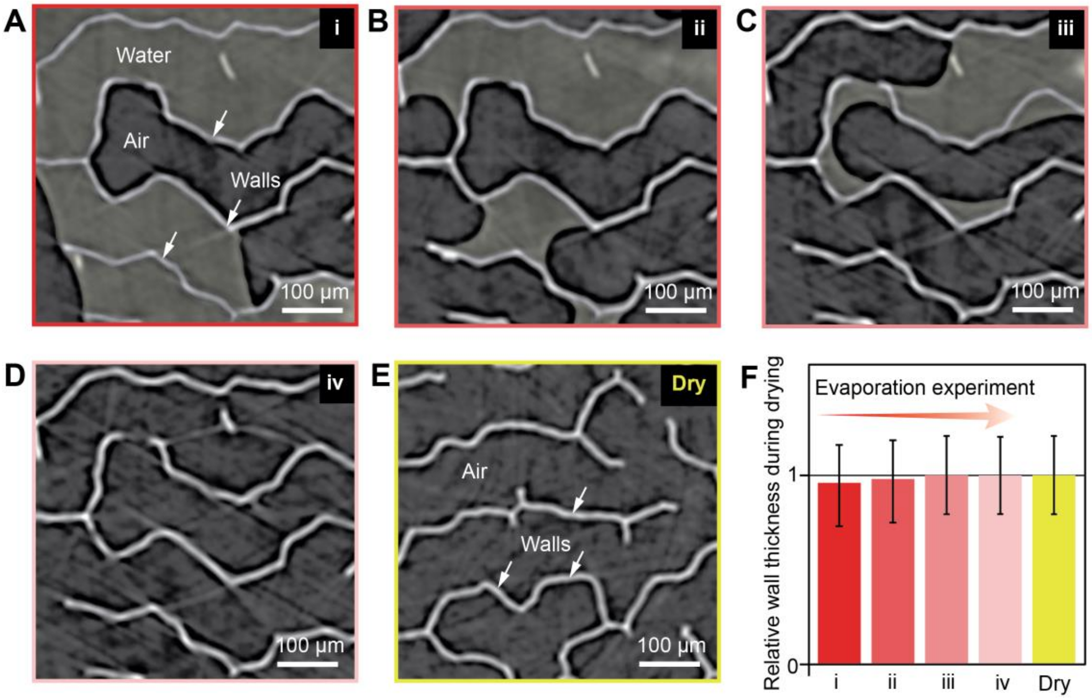

Fig. S2. Evaluation of wall thickness via *μ*-CT measurements of cuttlebone during an *in-situ* drying experiment. (*A*-*D*) *μ*-CT reconstructed slices of a wet sample at different drying stages. The entrapped water as highlighted gradually reduces its volume. (*E*) A reconstructed slice of a fully dried sample. (*F*) The measured relative wall thickness of (*A*-*E*) with error bars indicating the standard deviations, where the wall thickness of the fully dried sample is used as a reference.

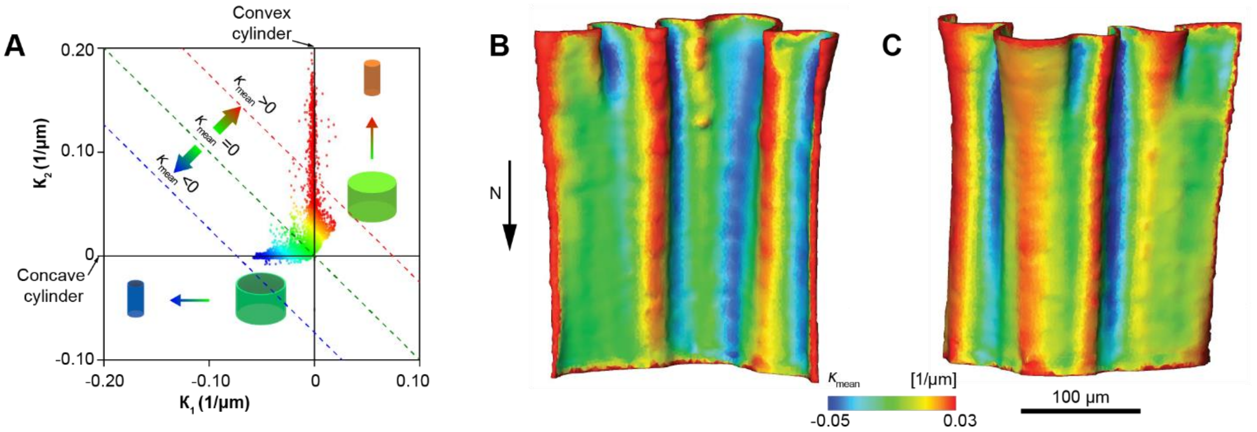

Fig. S3. Analysis of surface curvature distribution of a single wall. (*A*) Scatter plot of the principal curvature distributions (K_1 and K_2), where each data point is colored with the corresponding value of the mean curvature (K_{mean}). (*B*-*C*) Mean curvature distribution on (*B*) one side and (*C*) the opposite side of the wall.

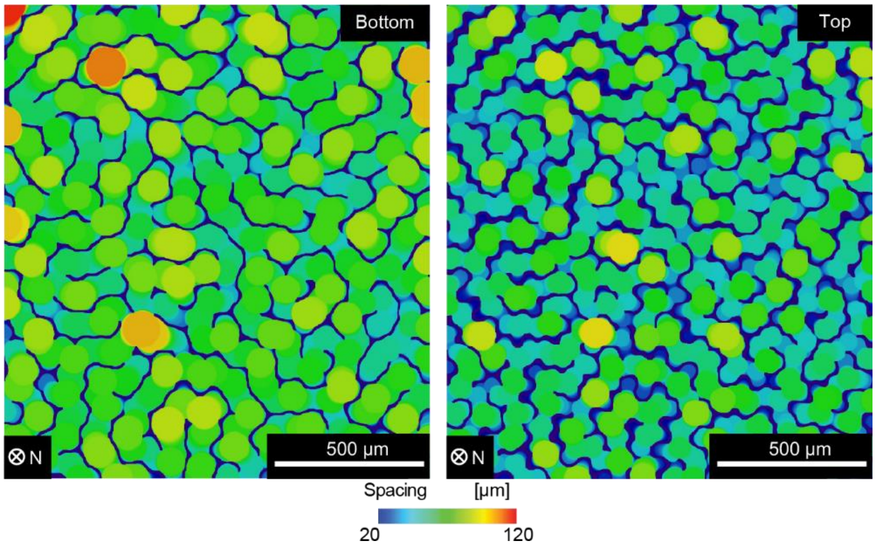

Fig. S4. The distribution maps of wall spacings at the bottom (left) and the top (right) of a chamber.

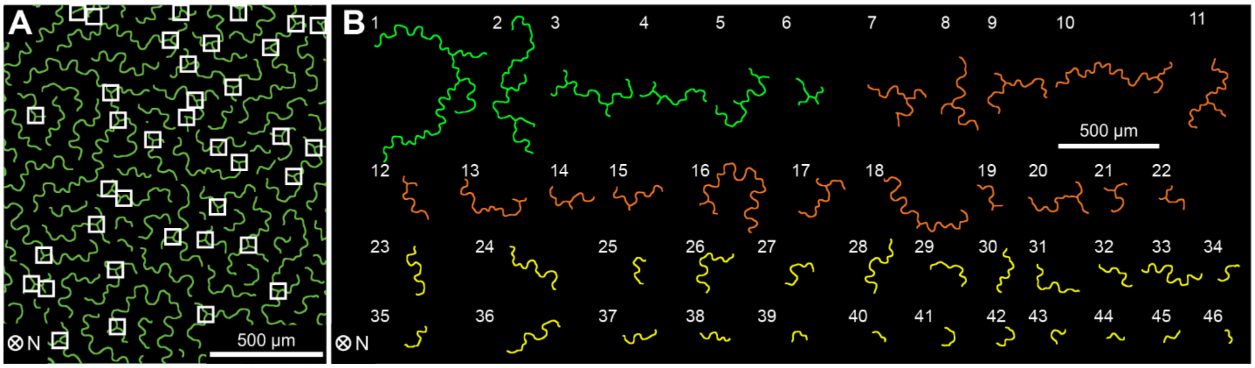

Fig. S5. Analysis of the triple junctions of the walls. (*A*) A representative labyrinthine pattern of the walls, where their triple junctions are indicated by white boxes. (*B*) Profiles of the walls with two triple junctions (1-6), one triple junction (7-22), and without triple junctions (23-46) in (*A*).

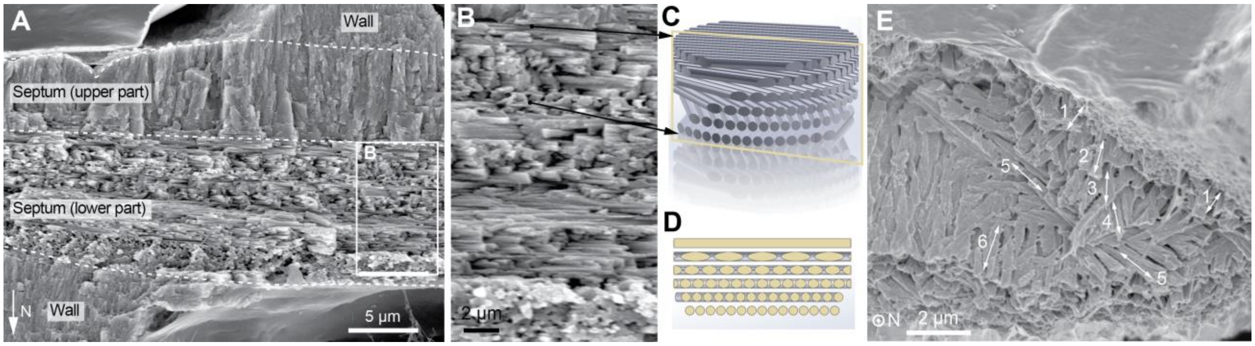

Fig. S6. The rotating plywood structure in the septum of a cuttlebone. (*A*) SEM image showing the double-layered structure of the septum. (*B*) Enlarged image of the white box marked in (*A*) where periodic variation in the morphology of the fractured fibers is observed. (*C*) A 3D model of the rotating plywood structure. (*D*) Cross-section view of the rotating plywood structure cut along the plane highlighted in (*C*). (*E*) SEM image showing the gradual change of the fiber orientation (arrows) in the vertical direction. The number 1-6 mark the different layers of fibers in the N direction.

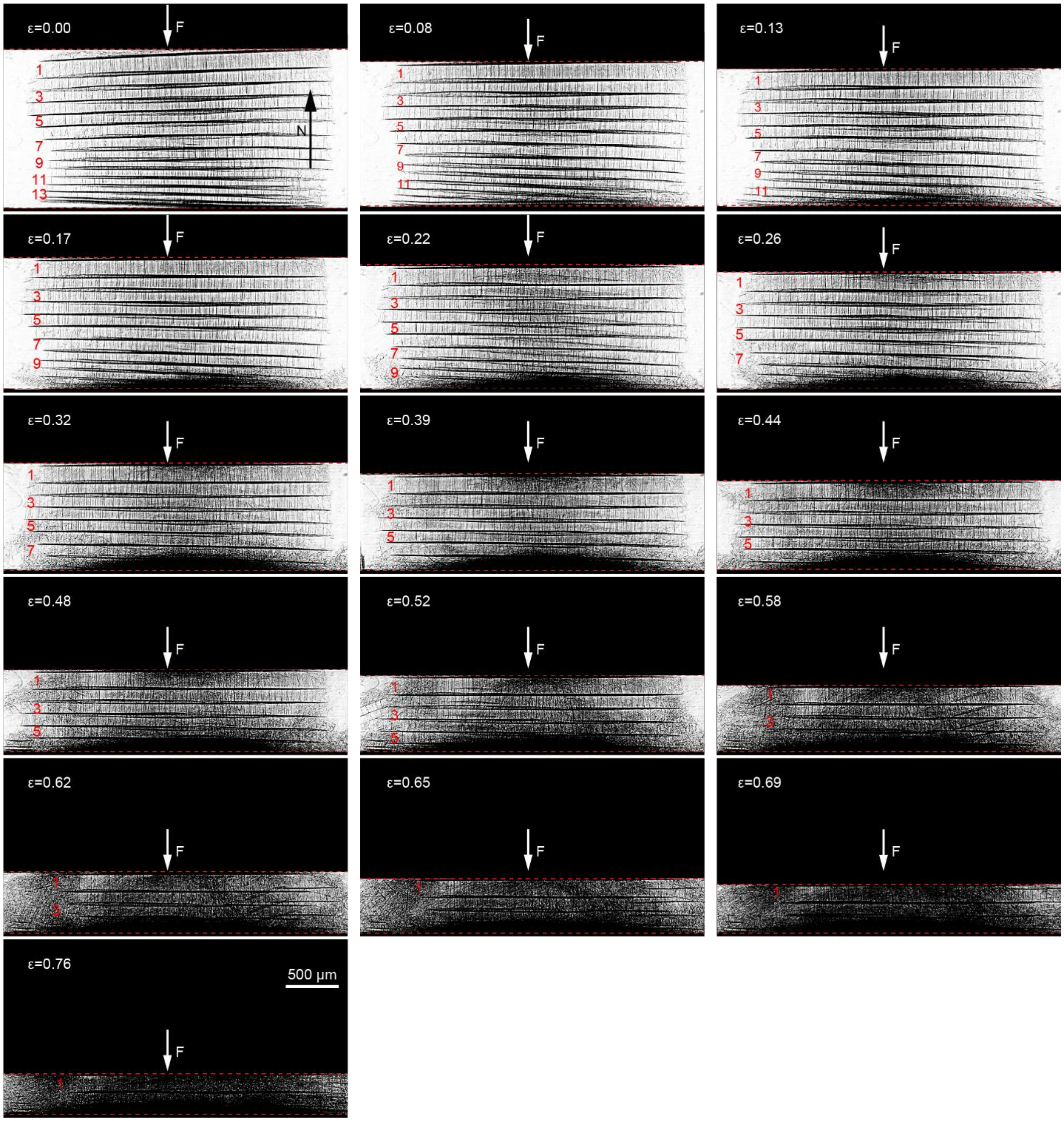

Fig. S7. X-ray projection images of a cuttlebone sample at different deformation stages during a typical *in*-*situ* compression test. The structure fractured via a chamber-by-chamber process from the sample bottom to top.

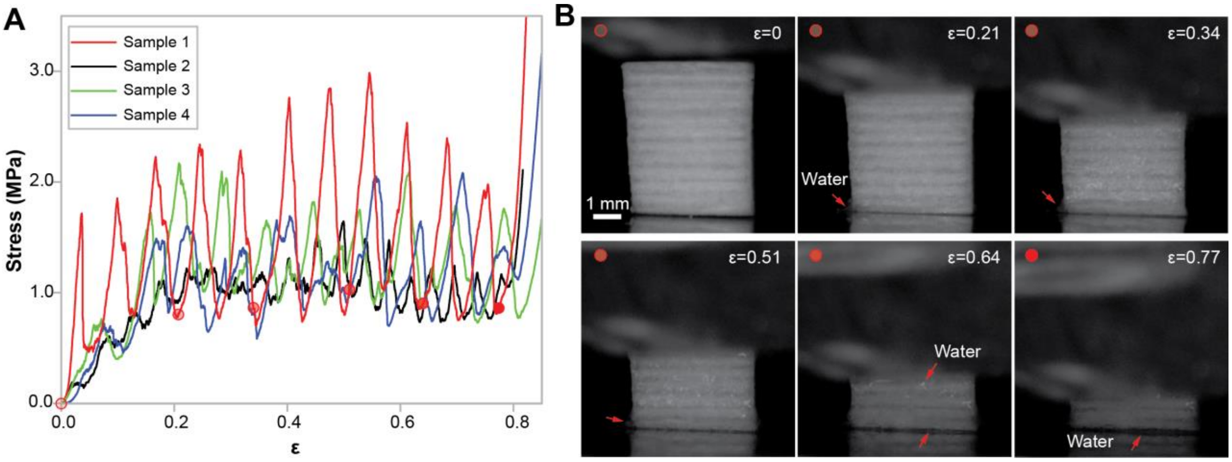

Fig. S8. *Ex-situ* compression tests on wet cuttlebone samples. (*A*) Stress-strain curves and (*B*) corresponding snapshots showing the deformation process for sample 1. Red arrows mark the locations of water squeezed out from the sample during compression.

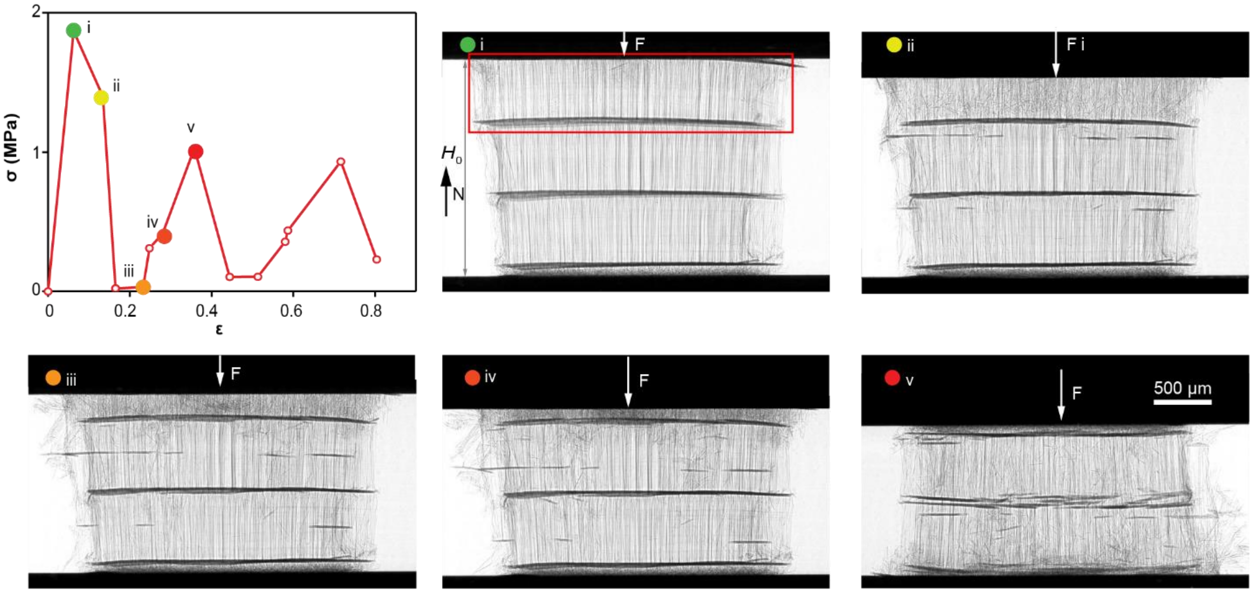

Fig. S9. The stress-strain curve and corresponding X-ray projection images of a cuttlebone sample during an *in-situ* synchrotron-based μ-CT compression test.

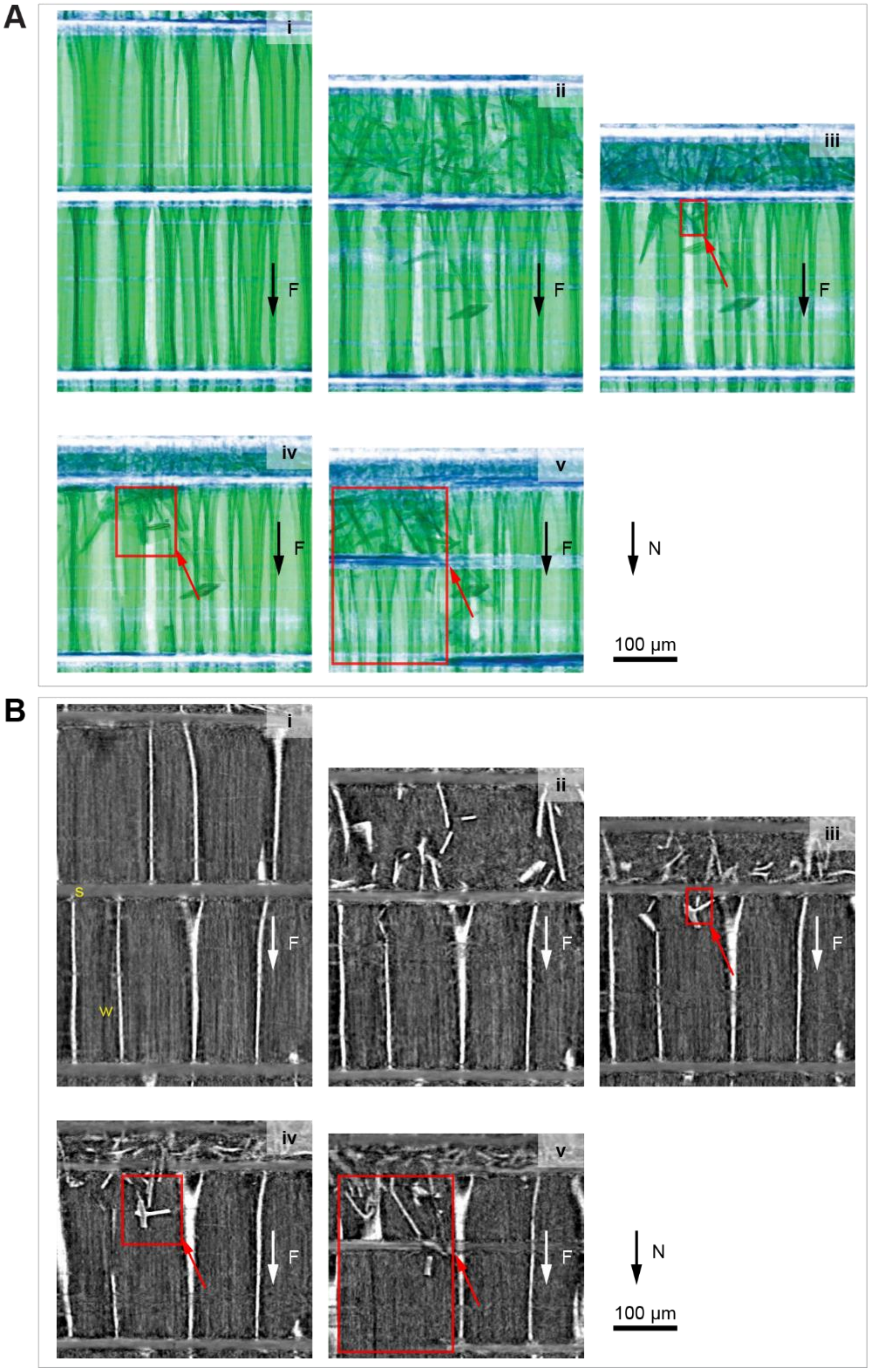

Fig. S10. Enlarged view of the deformation process of two adjacent chambers during an *in-situ* synchrotron-based *μ*-CT compression test. (*A*) Volume renderings and (*B*) corresponding vertical slices of the reconstructed two adjacent chambers at five deformation stages. Red arrows and red boxes indicate the local penetration of a septum and subsequent expansion in the fractured zone, respectively.

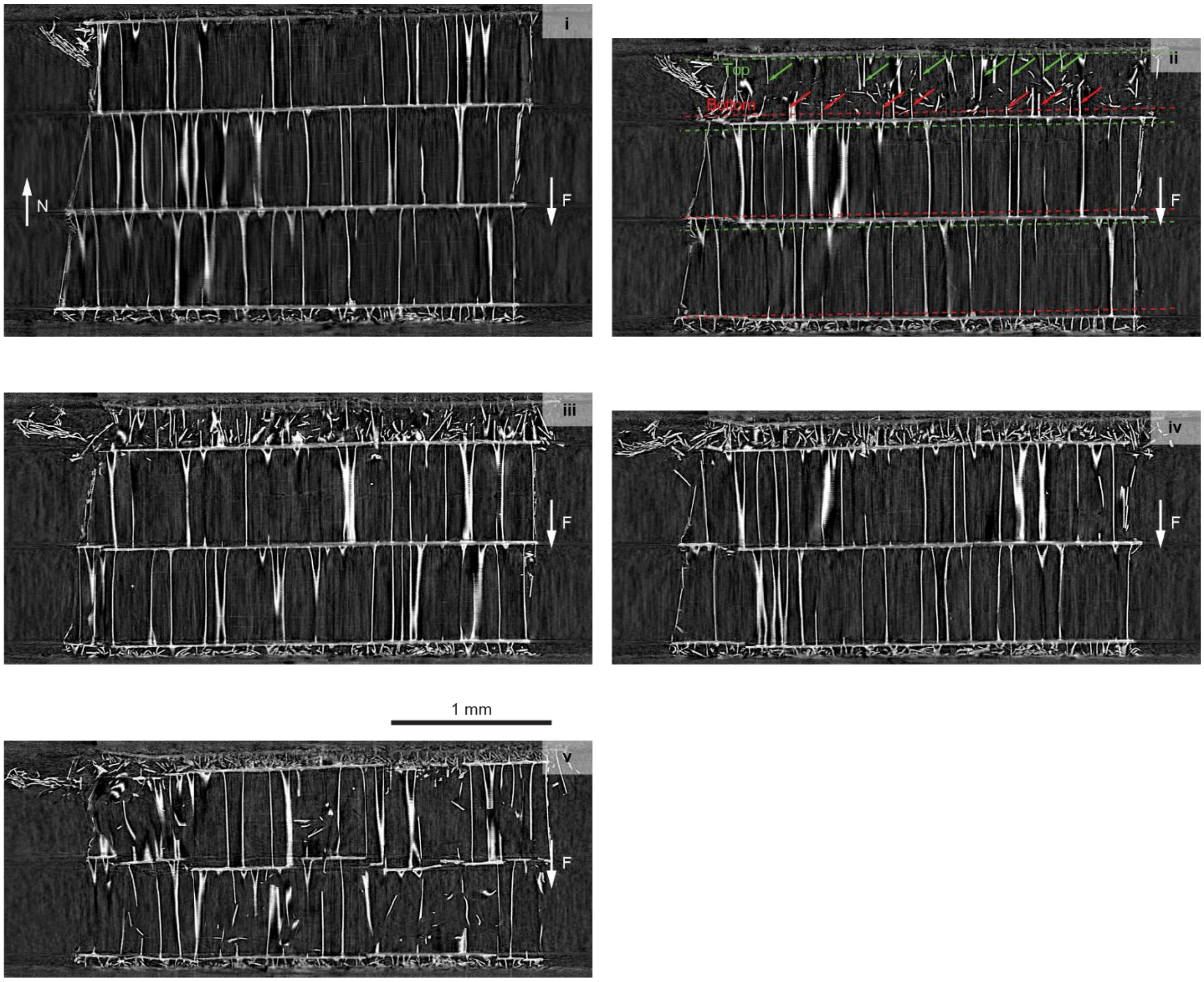

Fig. S11. Reconstruction slices of a cuttlebone sample at different stages of deformation during an *in-situ* compression test. The top and bottom parts of the fractured walls are indicated with green and red arrows, respectively.

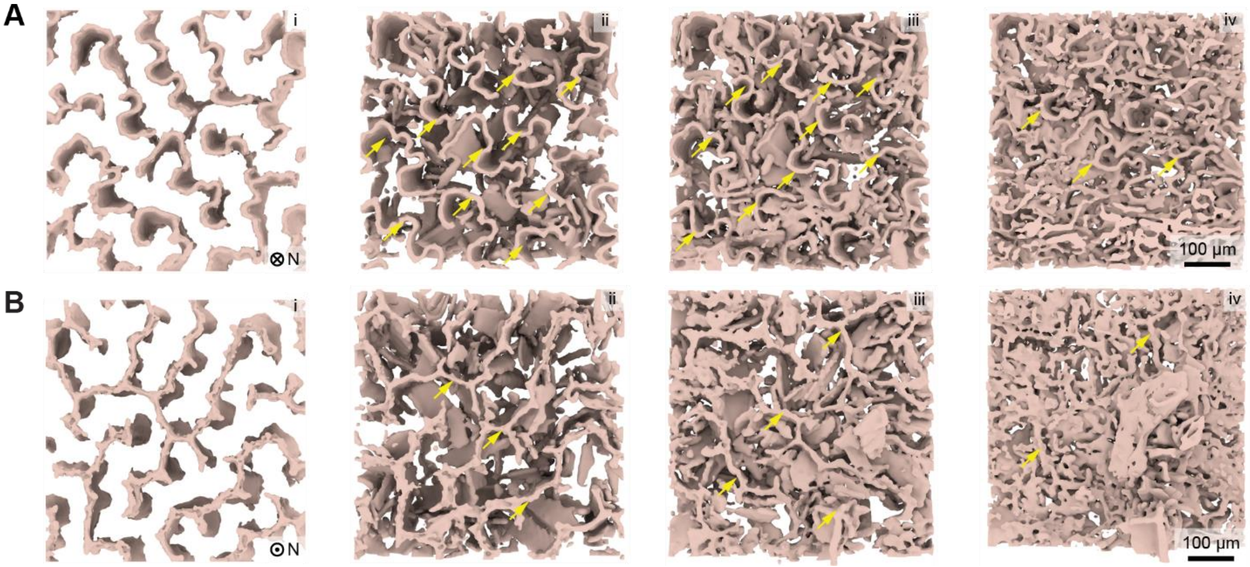

Fig. S12. 3D renderings of a chamber at different fracture stages on (A) the wavy side (wall top) and (B) the straight side (wall bottom). Note that the wall-septa connections on the wavy side are relatively more intact in comparison to the straight side at the same stage. The yellow arrows indicate the locations where the wall-septa connections are less damaged.

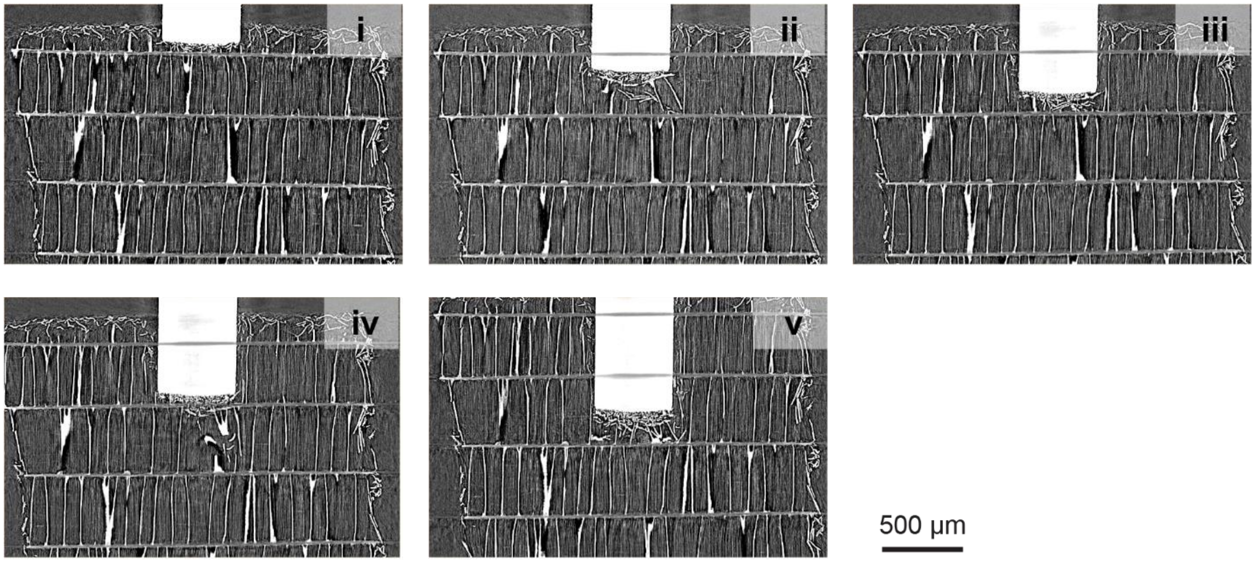

Fig. S13. Vertical reconstruction slices at five deformation stages during an X-ray *in-situ* indentation experiment with a flat-punch tungsten tip (white region).

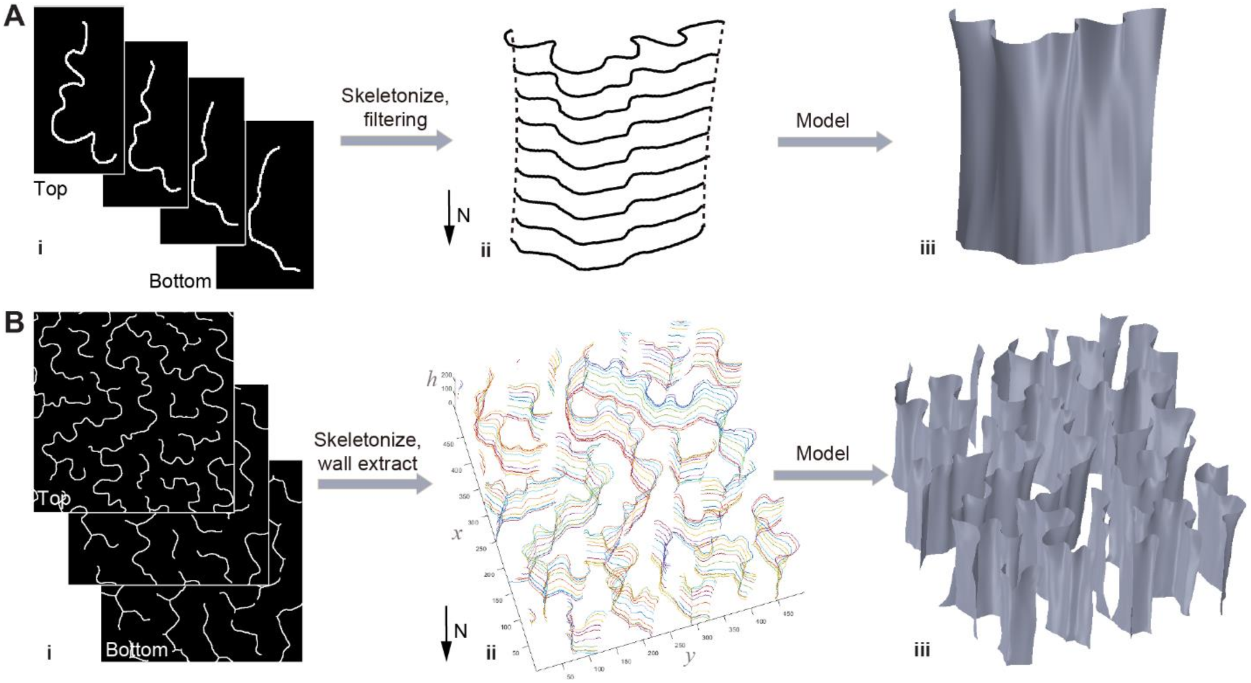

Fig. S14. Geometric modeling of (*A*) walls and (*B*) chambers based on reconstructed slices from $\mu\text{-}CT$ scans. The reconstructed slices are binarized, skeletonized, and then filtered to remove noise introduced during voxelization. The resultant geometric center-lines of the walls at varying heights are shown in the second column. These center-lines are then swept in Solidworks to form the wavy walls. Thickness is then assigned to produce solid models.

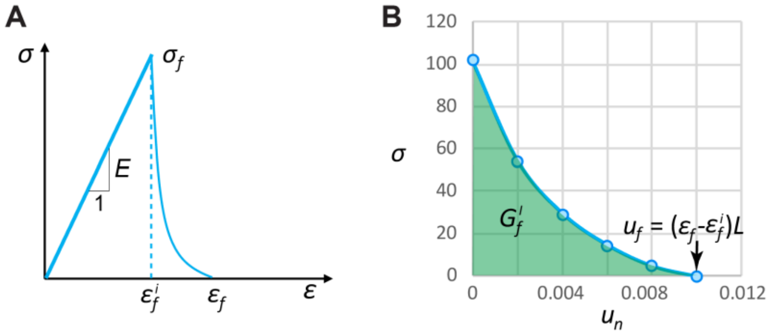

Fig. S15. (*A*) The fracture of walls in the simulation is realized by including a brittle fracture model together with element deletion. (*B*) To reduce mesh sensitivity, the fracture model is based on the mode I fracture toughness with $G_f^I = 0.71\ \mathrm{J/m^2}$. The stress-strain response (ε_f^i, the strain of damage initiation and ε_f, the strain of failure) and failure displacement (u_f) are then calculated based on the mesh size (L). The post crack initiation performance is assumed to follow a power law. Models with different mesh sizes are compared and verified to gain consistent stress-strain responses. The constituent properties of the biogenic aragonite used in simulation are E = 51 GPa, v = 0.3, and σ_f = 102 MPa.

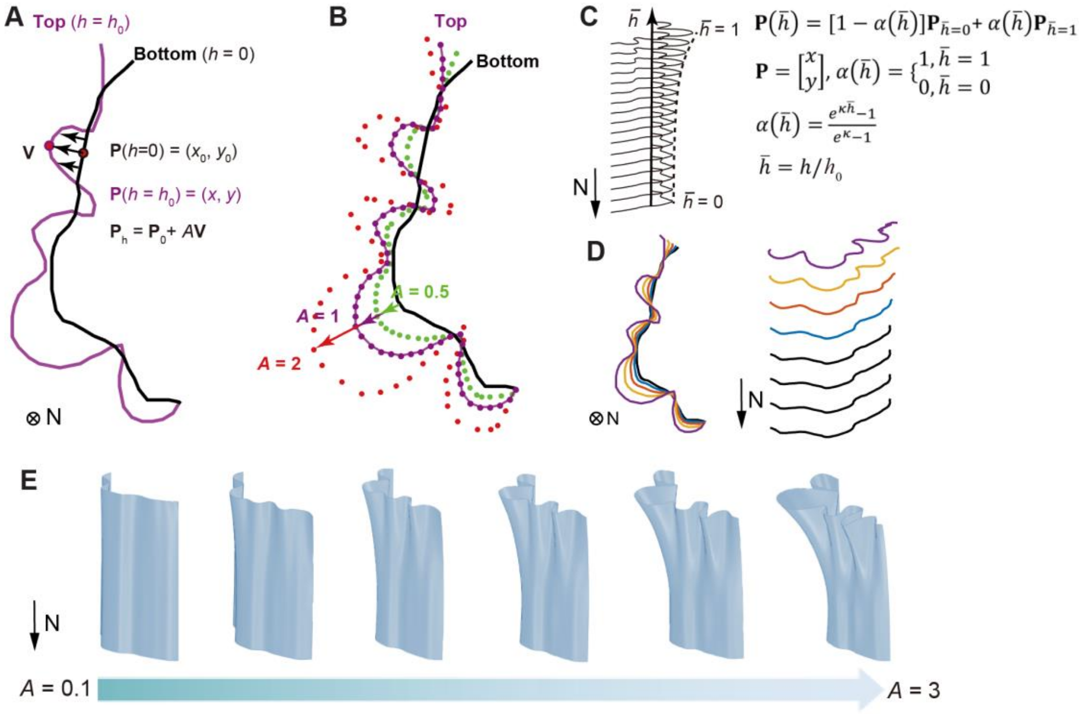

Fig. S16. The mathematical model used to describe the shape of the walls. Walls with different waviness are constructed with the same bottom profile but varying top profiles. The cross-section length of each wall is assumed to follow an exponential equation in the form of Eq. 1 in the main text. (*A*) Mathematical description of walls with different waviness amplitudes, $\mathbf{P}_{h=h_0} = \mathbf{P}_{h=0} + A \cdot \mathbf{V}$**,** where h is height and h_0 is the total height of the wall. The top profile of a wall ($\mathbf{P}_{h=h_0}$) is modeled as the addition of a vector ($A \cdot \mathbf{V}$) to the bottom profile ($\mathbf{P}_{h=0}$). (*B*) Walls with different top profiles, the amplitudes are A = 0.5, 1, and 2, respectively. (*C*) The wall is modeled by function $\mathbf{P}(\bar{h}) = [1 - \alpha(\bar{h})]\mathbf{P}_{\bar{h}=0} + \alpha(\bar{h})\mathbf{P}_{\bar{h}=1}$, with $\bar{h}$ defined as $\bar{h} = h/h_0$. (*D*) A resultant wall. (*E*) Walls with varying waviness amplitudes, the wall thickness is adjusted to maintain the same amount of solid material for different walls.

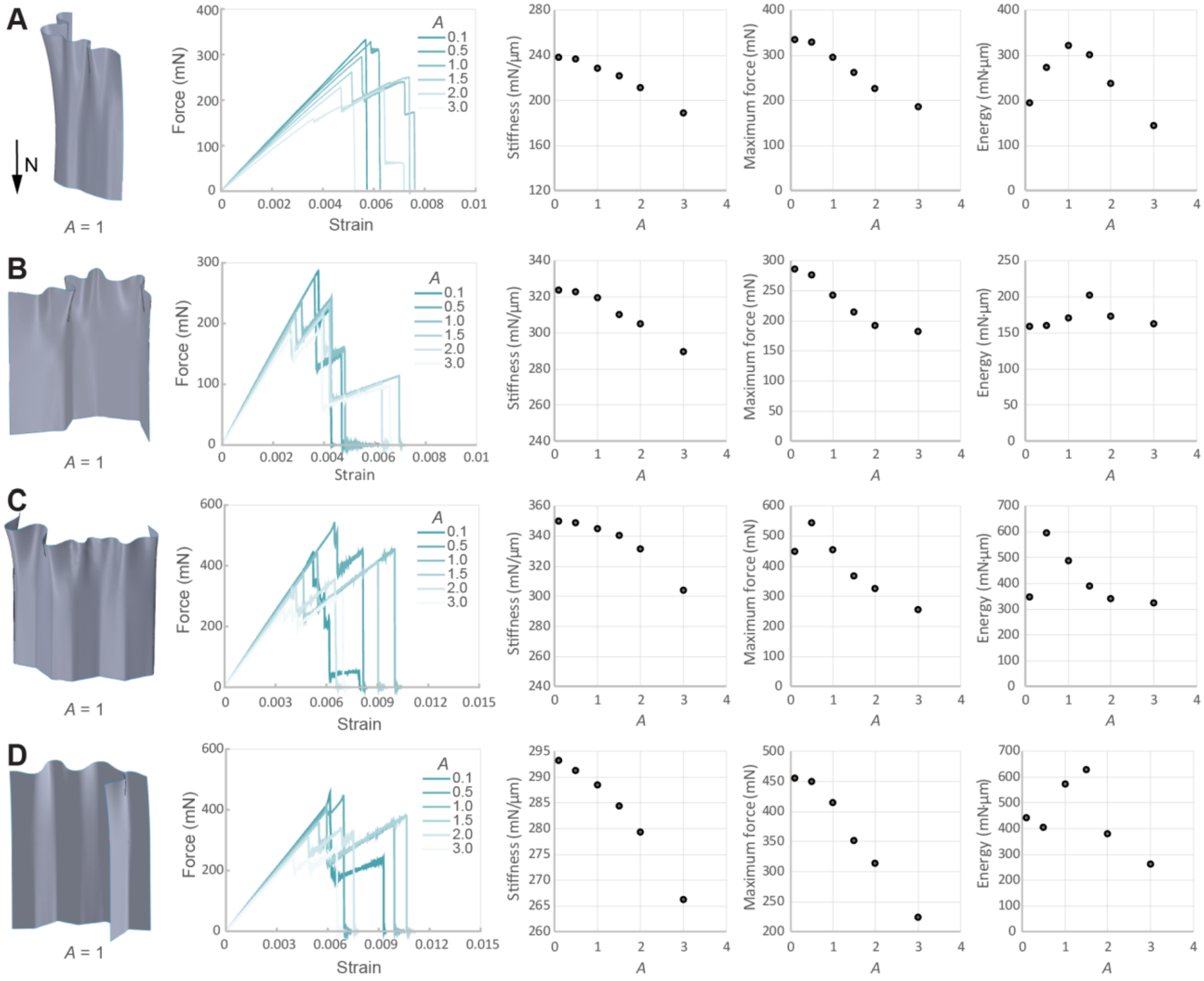

Fig. S17. The effect of waviness amplitude on the mechanical performances of single walls. Walls with four different geometries are studied. Simulations are performed on walls with waviness amplitude *A* = 0.1~3, *A* = 1 corresponds to the *μ*-CT based walls. General trend: walls with small waviness (e.g., *A* = 0.1) have a higher stiffness but tend to break catastrophically, while walls with excessive waviness (e.g., *A* = 3) have significantly degraded stiffness and strength. The optimal *A* is in the range of 0.5~1.5, demonstrating that the waviness of the cuttlebone is optimized statistically. The failure stress decreases at increasing waviness. This trend shows that the walls become weaker at increasing second moment of area, which indicates that buckling is not the mechanism that controls failure.

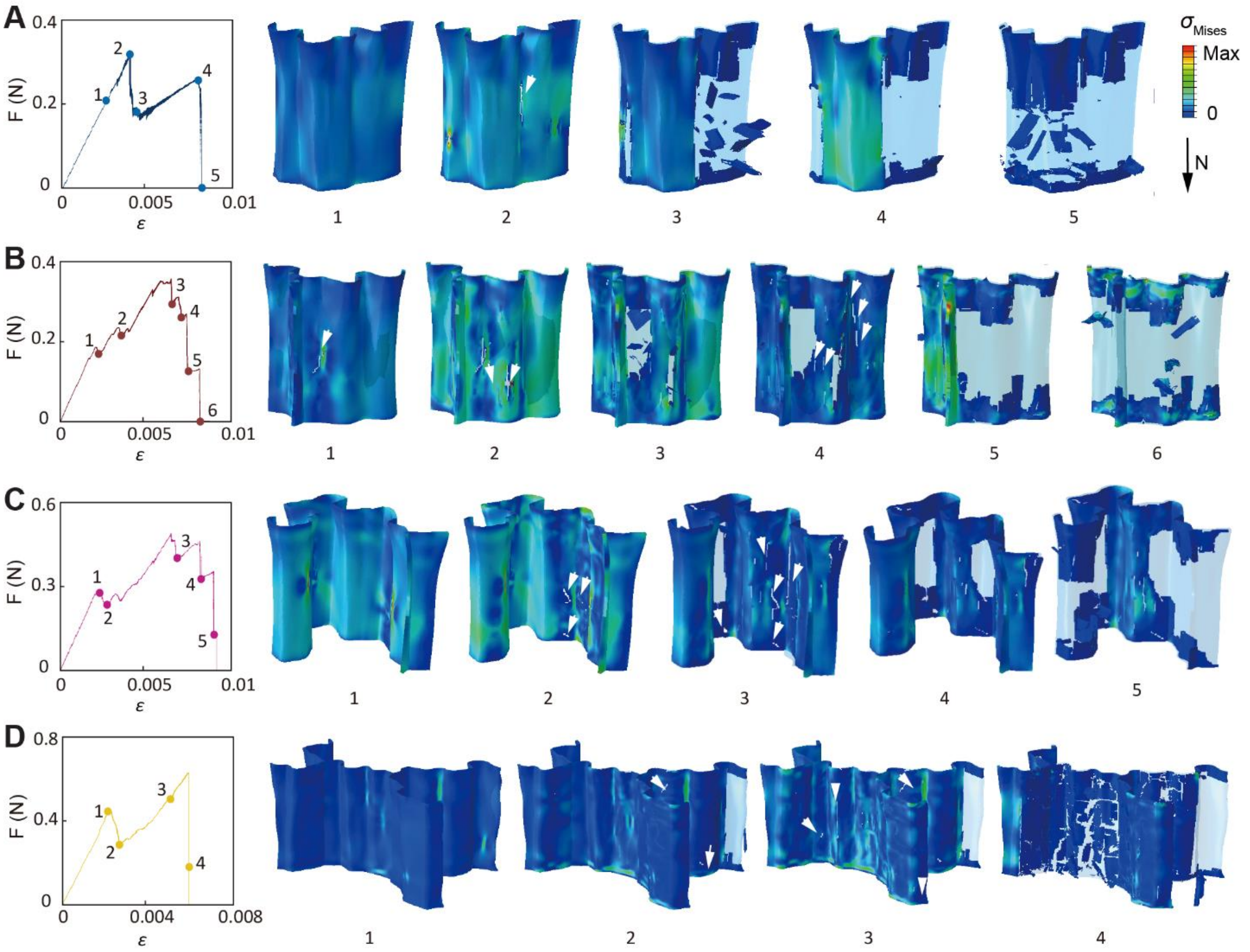

Fig. S18. Simulation results of the fracture process of walls with four different geometries (*A*-*D*). The wall geometries are reconstructed from μ-CT data utilizing the method described in Fig. S14. The fracture of the wall happens in a progressive manner, where uneven stress distribution leads to the failure of different wall segments at different strains. Each wall fracture corresponds to a stress drop in the stress-strain curve.

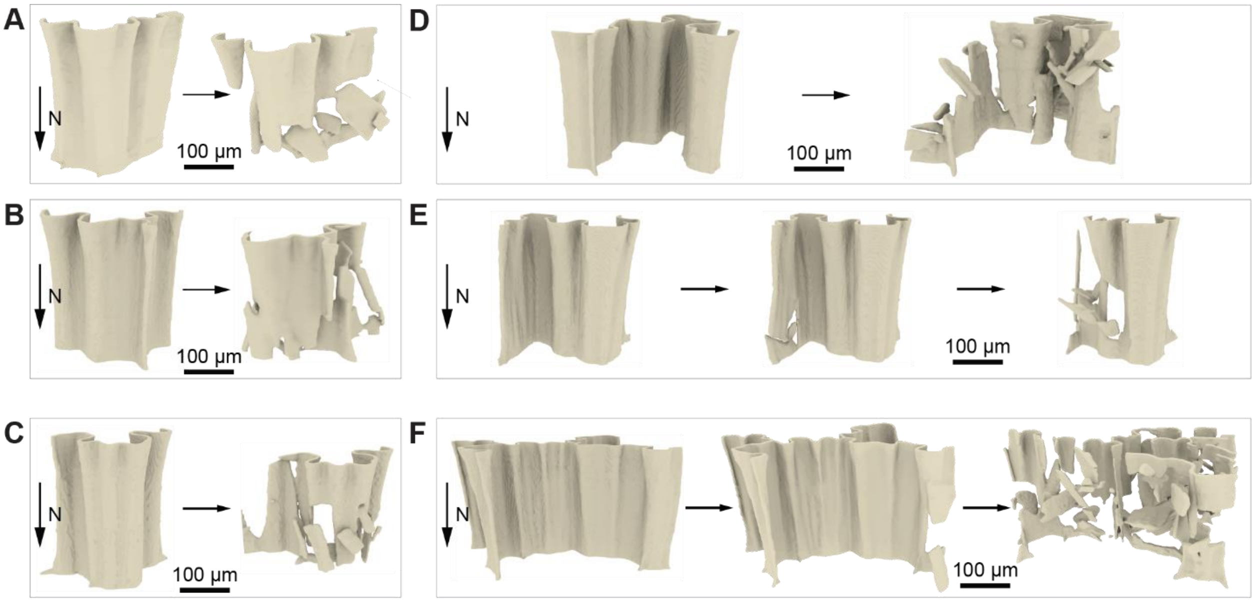

Fig. S19. Representative wall morphologies before and after fracture reconstructed from *in-situ* μ-CT compression experiments.

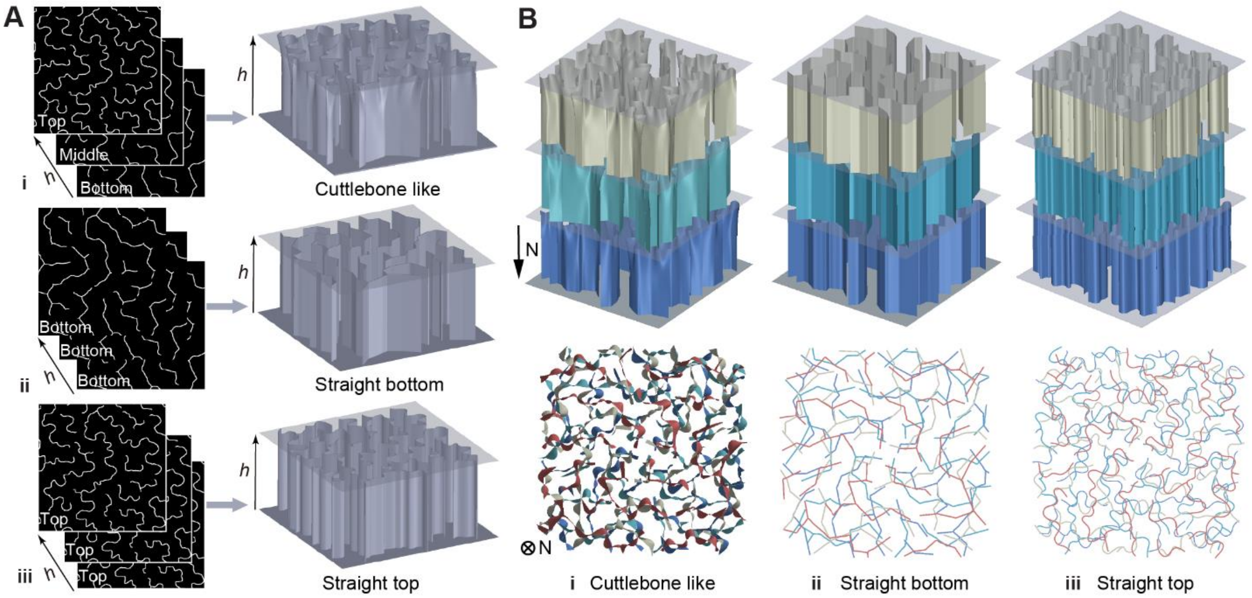

Fig. S20. The construction of chambered models. (*A*) single-chamber model and (*B*) multiple chamber model based on reconstructed slices from μ-CT scans.

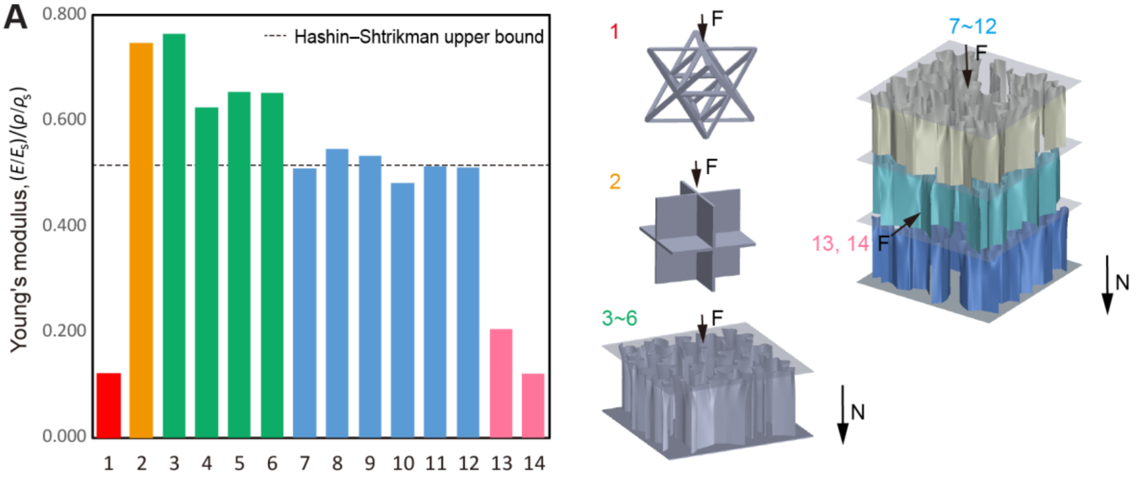

B

	Structure	E_{eff} (MPa)	E_{eff}/E_s	$(E_{eff}/E_s)/(\rho_{eff}/\rho_s)$
1	Oct-truss	435	0.00853	0.122
2	Cubic foam	2664	0.05224	0.746
3	One chamber, cuttlebone $t_s = t_w$	2732	0.05357	0.765
4	One chamber, cuttlebone $t_s : t_w = 6.1{:}3$	2231	0.04375	0.625
5	One chamber, straight 1 $t_s : t_w = 6.1{:}3$	2339	0.04586	0.655
6	One chamber, straight 2 $t_s : t_w = 6.1{:}3$	2332	0.04573	0.653
7	Multichamber, cuttlebone $t_s : t_w = 6.1{:}3$ $E_s = E_w$	1819.4	0.03567	0.510
8	Multichamber, straight 1 $t_s : t_w = 6.1{:}3$ $E_s = E_w$	1954.23	0.03832	0.547
9	Multichamber, straight 2 $t_s : t_w = 6.1{:}3$ $E_s = E_w$	1905.34	0.03736	0.534
10	Multichamber, cuttlebone $t_s : t_w = 6.1{:}3$ $E_s : E_w = 29.6{:}51$	1725.9	0.03384	0.483
11	Multichamber, straight 1 $t_s : t_w = 6.1{:}3$ $E_s : E_w = 29.6{:}51$	1830.983	0.03590	0.513
12	Multichamber, straight 2 $t_s : t_w = 6.1{:}3$ $E_s : E_w = 29.6{:}51$	1829.471	0.03587	0.512
13	Multichamber, cuttlebone $t_s : t_w = 6.1{:}3$ $E_s = E_w$	736.114	0.01443	0.206
14	Multichamber, cuttlebone $t_s : t_w = 6.1{:}3$ $E_s : E_w = 29.6{:}51$	431.5376	0.00846	0.121

Fig. S21. Cuttlebone structure as an ultra-stiff design. Stiffness comparison between the cuttlebone-based structures, an octet truss lattice, and a cubic metafoam. The stiffness of the single-chamber cuttlebone structure is close to that of the cubic foam. The 3-chamber cuttlebone structure is 3 times stiffer than the octet lattice and is ~30% less stiff than the cubic foam, close to the maximum stiffness of an isotropic lattice (H-S upper bound). Structure #1~3 are assumed to have the same thickness and material composition for bioinspired design considerations. For structure #4~8, septa are assumed to be softer but thicker than the vertical walls (the properties of wall unchanged and the stiffness of septum is reduced). That is, $E_s : E_w$ = 29.6:51, $t_s : t_w$ = 6.1:3, where E and t are Young's modulus and the wall thickness respectively, the subscript s and w denote septum and wall respectively. All structures share the same volume fraction. The specific stiffness of the cuttlebone can be estimated from the simulation no. 10, which is most close to the chambered structure of cuttlebone. By dividing the stiffness by the density, the specific stiffness of cuttlebone is calculated to be 8.4 MN·m/kg.

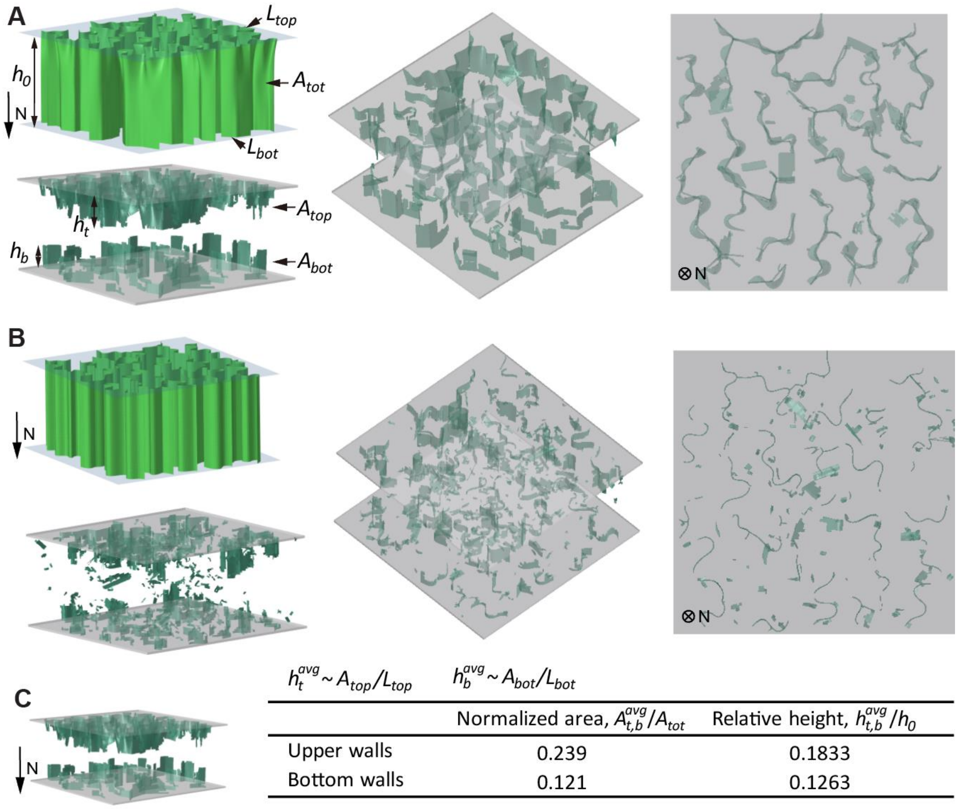

$h_t^{avg} \sim A_{top}/L_{top}$ $h_b^{avg} \sim A_{bot}/L_{bot}$

	Normalized area, $A_{t,b}^{avg}/A_{tot}$	Relative height, $h_{t,b}^{avg}/h_0$
Upper walls	0.239	0.1833
Bottom walls	0.121	0.1263

Fig. S22. Post fracture morphology comparison between single chambers with wavy walls (*A*) and with straight walls (*B*). The wavy structures exhibit more progressive failure and fracture into larger pieces. More specifically, the fractured upper walls of the wavy structures generally have a greater height than the bottom part, $h_t > h_b$. $A_{top}$and A_{bot} refer to the total areas of the walls in the top and bottom portions respectively. $L_{top}$and L_{bot} refer to the length of the wall profiles on the top and bottom septa respectively. The post-fracture measurements reveal the asymmetric fracture of the wavy walls, with h_t/h_0= 0.1833 and h_b/h_0 = 0.1263.

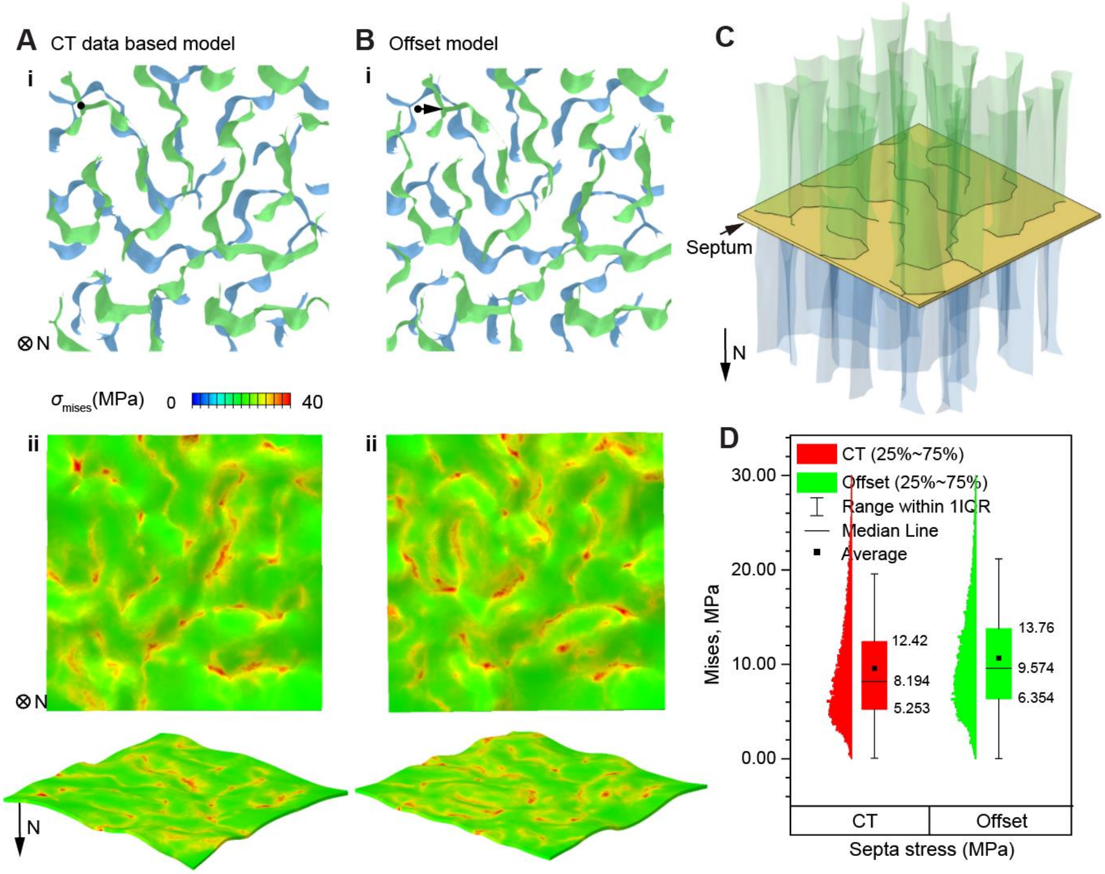

Fig. S23. Effect of the wall overlaying pattern on the septa stress. (*A*) The original wall overlaying pattern based on μ-CT scan. (*B*) The wall overlaying pattern with 50 µm offset based on the original μ-CT model. The offset model exhibits larger septum deformation than the original μ-CT based pattern (displayed with x50 magnification), indicating that an improper interlayer packing is disadvantageous to the integrity of septa. (*C*) 3D view of the original wall overlaying pattern on the top and bottom of a septum, with the top and bottom walls highlighted. (*D*) Statistics of stress distribution on the septa. The offset model exhibits 16.8% larger average Mises stress than the original μ-CT based model.

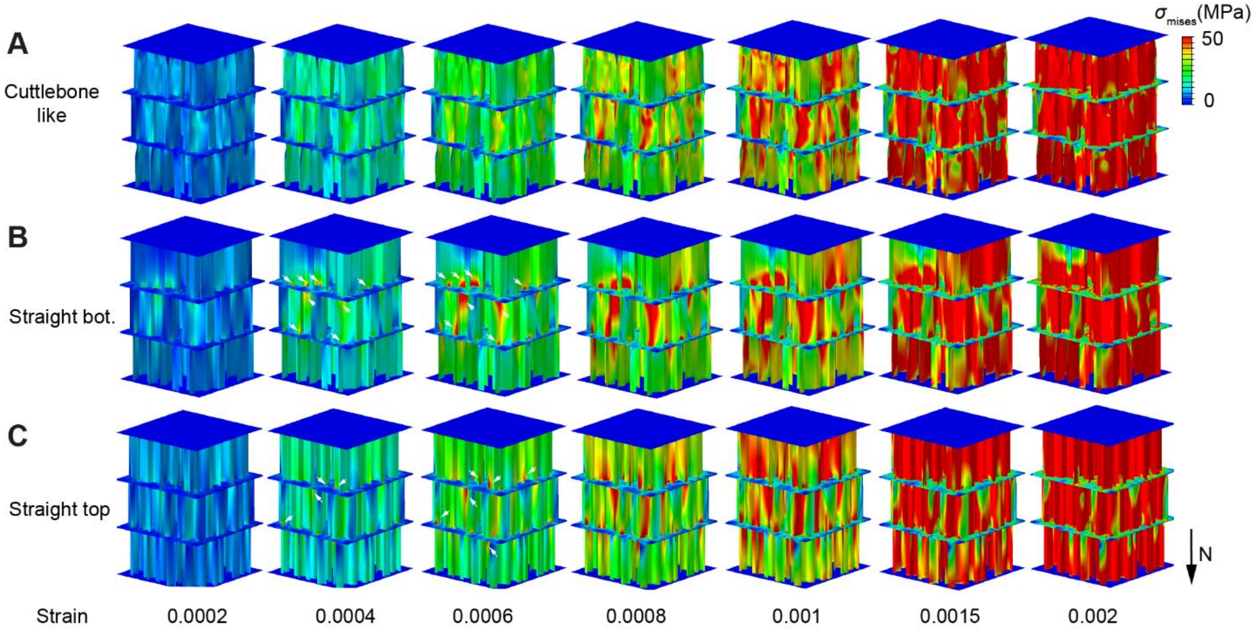

Fig. S24. Stress distribution comparison between the three-chamber models with (*A*) wavy walls, (*B*) straight walls based on the bottom profile, and (*C*) straight walls based on the top profile under increasing compressive strains (see Fig. S20 for methods of generating these models). As marked by the white arrows (high-stress regions), the straight wall based models exhibit much more significant stress concentration than the wavy wall based model. Unfavorably, these stress concentration regions are near the septa, which make the septa prone to premature penetration.

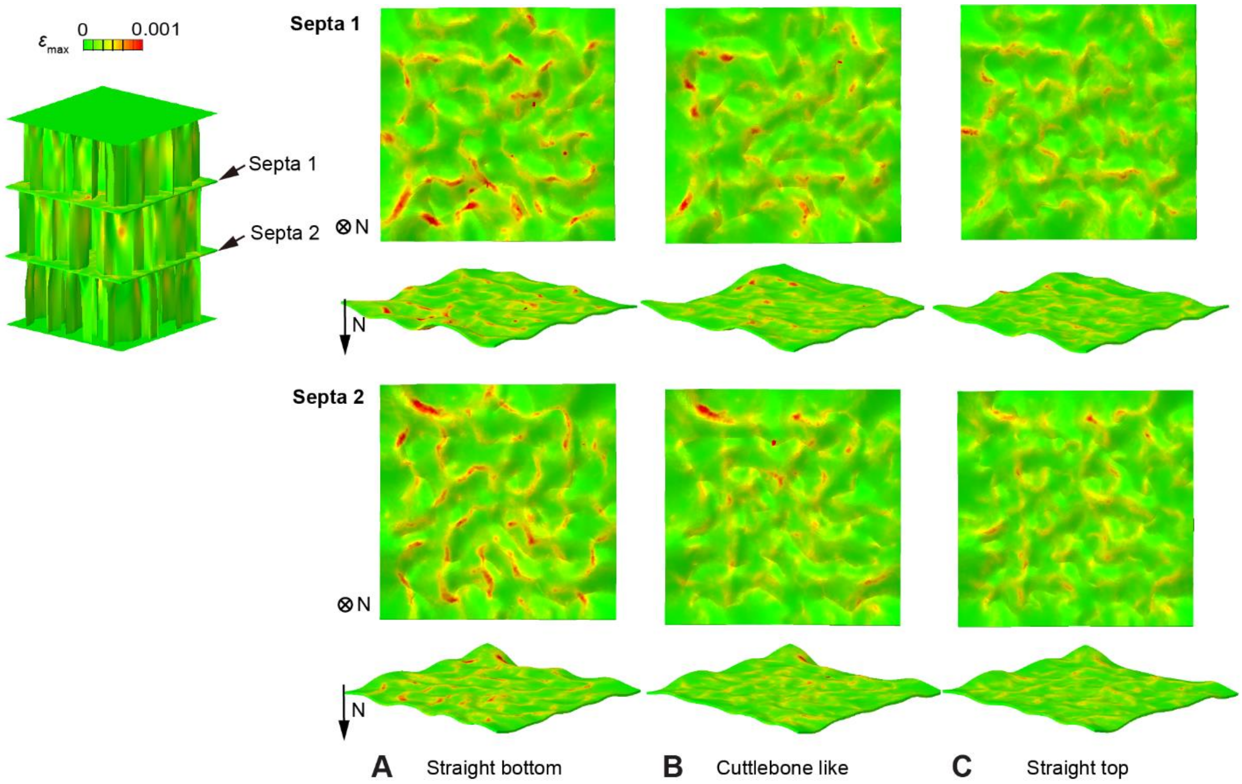

Fig. S25. A comparison of stress distributions on the septa between the wavy wall based model and the straight wall based models. The wavy wall based model (*B*) presents reduced stress compared to the straight wall bottom pattern based model (*A*), but larger stress than the straight wall top pattern based model (*C*).

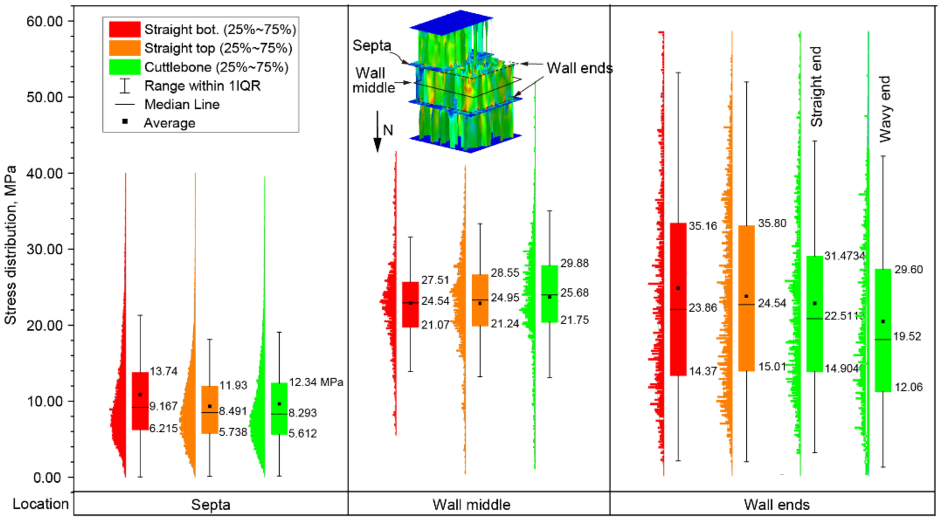

Fig. S26. Statistical analysis of the stress distributions on the septa, in the middle portion of the walls and at the ends of the walls. Compared to the straight wall based structures, the wavy wall based structure presents reduced stress on the septa and at the ends of the walls, but increased stress in the middle portion of the walls. Note that 1. The reduced stress on septa improves septa integrity. 2. The improved stress at the middle portion of the walls localizes wall fracture to the middle region. 3. The asymmetric stress distribution at the two wall ends of the wavy wall facilitates asymmetric fracture. Also note that 1IQR represents the range within 1 interquartile range (minimum + 1IQR ~ maximum data – 1IQR).